Tribology International 193 (2024) 109349

Contents lists available at ScienceDirect

Tribology International

journal homepage: www.elsevier.com/locate/triboint

Investigation of failure modes and material structural responses of nanographite coatings on single-crystal silicon by nanoscratching

Fabian Brüssel, Weihai Huang, Jiwang Yan *

Department of Mechanical Engineering, Faculty of Science and Technology, Keio University, 3–14-1 Hiyoshi, Kohoku-ku, Yokohama 223–8522, Japan

ARTICLE INFO

Keywords:
Nanoscratching
Nanographite coatings
Single-crystal silicon
Failure modes
Microstructural changes

ABSTRACT

The failure modes of a nanographite-on-silicon system and the effects of the coating on the load-induced phase transformation of the silicon substrate were investigated using a series of nanoscratching tests with a spherical diamond indenter. The critical normal load for the failure of the nanographite coating was determined based on the thickness of the coating. When the load increased beyond the critical point, cracks, press spallation, and lift spallation were observed, and the silicon substrate underwent a phase transformation from the original crystalline phase to a mixture of amorphous, Si-III and Si-XII phases. For a thin coating, the silicon substrate was free of phase transformation owing to the coating protection. These findings provide guidance for glass molding and other applications.

1. Introduction

Thin films and coatings are suitable for a wide range of applications. For example, in optical technology, the application of optical thin films has expanded the design possibilities of optical components. Single- or multilayered thin films can modify the optical properties of components to the desired quality [1,2]. Coatings can also reduce friction and adhesion and enhance heat conduction, which is essential for improving the performance of chain drives in the mechanical systems [3], cutting tools in the machining industry [4,5], and artificial joints in the medical technology fields [6]. The application of coatings improves the performance and reliability of advanced engineering components, thereby significantly benefiting the industry in terms of capital. In recent years, a new and breakthrough application of coatings has been rapidly developing in high-precision glass molding field, which involves the use of anti-sticking coatings on the micro-structured surfaces of molds to extend their lifespan and create a smooth glass surface without the need for additional polishing [7]. Silicon is one of the attractive materials for making molds, because the micro/nano manufacturing technologies based on Si wafers have been well developed, such as lithography, laser processing, and diamond cutting. Additionally, silicon is chemically stable and hard at high temperatures. However, severe adhesions between Si and glass can occur at elevated temperatures due to anodic bonding and chemical bonding. This significantly limits the use of Si as a mold material for glass molding. The solution to overcome this issue has been the deposition of thin films and coatings, such as Ru [8] and IrRe [9], on silicon molds. Compared to the deposition of precious metals with complicated devices, deposition of nanographite is more accessible in terms of equipment, and the cost is lower due to the abundant carbon source. In addition, nanographite has high thermal conductivity, high strength, and low surface friction, which is an ideal coating material as a protective layer on silicon molds. Recently, nanographite has been successfully coated on single-crystal Si using the atmospheric pressure chemical vapor deposition (APCVD) process as an anti-adhesive protective layer, which eliminated the Si–glass adhesion at elevated temperatures in glass molding [10,11]. The nanographite coating layer is suitable owing to its versatility in replicating micro/nano structures, which was successfully demonstrated using molding experiments with micropillars and microlens arrays on glass [12]. During glass molding, a glass preform becomes a viscoelastic/plastic body at elevated temperatures and deforms and moves laterally relative to the mold surface when a pressing load is applied to the mold [13]. Thus, preforming is known as a process in which a tool scratches a mold with a nanographite coating. The thickness of the coating can be adjusted by varying the amount of silicone rubber and the reaction time [14]. However, the relationship between coating thickness and mechanical resistance remains unclear.

The mechanical properties of thin films and coatings, particularly the strength of the film-substrate interface, are crucial for their effectiveness, reliability, and service life when used under harsh conditions. To characterize the mechanical stability of the film-substrate system, the

* Corresponding author.
E-mail address: yan@mech.keio.ac.jp (J. Yan).

https://doi.org/10.1016/j.triboint.2024.109349
Received 3 November 2023; Received in revised form 23 January 2024; Accepted 28 January 2024
Available online 1 February 2024

nanoscratching method is an effective method that has been widely used for testing various thin-film materials [15,16]. For scratching on coatings of Si substrates, Beake et al. [17] assessed the durability of TiN/-Si_3N_4 coatings on Si substrates. The nanoscratching behavior was found to be influenced by the ratio of hardness (H) to elastic modulus (E) of the coating. Coatings with higher H/E showed a higher critical load for the elastic-plastic transition, thereby preventing failure from occurring in front of the tool. However, a higher H/E value may lead to unloading failures behind the tool. They also conducted scratching tests of TiFeN coatings on silicon and found that the thickness of the coating and the properties of the coating and substrate affected the deformation process parameters such as the critical load and failure mode[18]. Lee et al. [19] conducted ramp-load scratching tests to evaluate the adhesion properties of Ag and ZnO films coated on Si wafers fabricated by sputtering deposition and the sol-gel method. Li et al. [20] compared the micro/-nanomechanical and tribological characteristics of ultrathin amorphous carbon coatings on silicon fabricated using various deposition processes, including sputtering (SP), direct ion beam (IB), filtered cathodic arc (FCA), and plasma CVD. The coatings prepared by plasma CVD and FCA showed better scratch/wear resistance than those prepared by IB and SP, and thicker coatings exhibited better load-carrying capacities than thinner coatings. Although multiple nanoscratching studies have been conducted on various coating materials on Si substrates to characterize their mechanical properties and failure mechanisms, few studies have investigated the material response of Si substrates to mechanical loads. It has been acknowledged that uncoated silicon produces amorphous phases on its subsurface after nanoscratching [21–23]. In the nanoscratching of coatings on silicon, the effect of the coatings on the subsurface microstructural changes of the Si substrate remains unclear. In addition, the mechanical behavior of nanographite-coated single-crystal silicon fabricated by APCVD, which is currently used in precision glass molding, remains unknown.

In this study, constant- and ramp-load nanoscratching tests were conducted on different thicknesses of nanographite coatings on single-crystal silicon to statistically investigate the overall response characteristics of nanographite coatings to mechanical loads and determine the threshold of coating failure. The surface morphology and subsurface microstructure of the scratched grooves were examined. The critical maximum load and failure modes of the nanographite coatings with different thicknesses were determined. The effects of the coatings on microstructural changes in Si substrates were revealed. The findings of this study provide guidance for the preparation of coated molds in the glass molding industry and other applications that use coating protection. In addition, it will elucidate the influence of coatings on the microstructural changes of Si substrates under mechanical loads.

2. Material and methods

2.1. Preparation of specimens

The specimens used for the nanoscratch tests were single-crystalline p-type (100) oriented silicon wafers coated with a thin layer of carbon. The silicon substrate has dimensions of 10 mm × 10 mm × 0.5 mm, and its surface roughness, prepared by a chemomechanical polishing process, is less than 0.5 nm Sa. The coating process was accomplished using APCVD in a high-temperature tube furnace (Xiamen Tmax Battery Equipment Ltd., China), and the experimental configuration is shown in Fig. 1(a). A liquid carbon source, anhydrous benzene (Hayashi Pure Chemical Ind., Led., Japan) with a purity of 99.9 % in a glass bubbler, and a Si source, silicone rubber, were used for a nanometer-thick carbon coating. A Si wafer and 0.5 g of silicone rubber was placed in a quartz tube with a length of 600 mm and diameter of 50 mm. An inert gas (Ar) was used to displace the residual air from the quartz tube and eliminate the oxidation effect at elevated temperatures during the coating process. The initial flow rate was maintained at 60 SCCM for 15 min and then reduced to 50 SCCM. The temperature was increased from ambient to

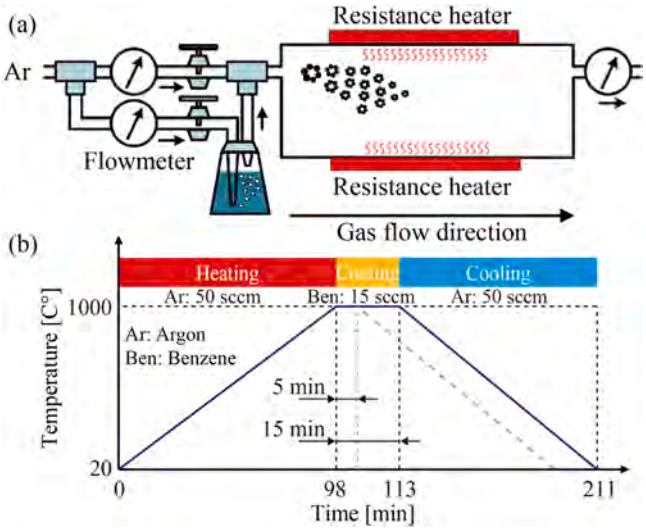

Fig. 1. (a) Hardware configuration of the high-temperature tube furnace; (b) temperature-time curves for the coating times of 5 and 15 min.

the reaction temperature (1000 ℃) with a constant heating rate (10 ℃/min). After the reaction temperature was reached, anhydrous benzene was introduced into the tube by blowing Ar as a carrier gas at 15 SCCM, and the shielding Ar gas was adjusted to 35 SCCM to ensure a constant flow rate. Then, the reaction temperature was maintained for 5 min and 15 min, respectively, and the quartz tube was gradually cooled down to ambient temperature (10 ℃/min), as depicted in Fig. 1(b). The surface morphology and thickness of the nanocarbon coatings could be controlled by adjusting the coating time. Fig. 2(a) shows the cross-sectional transmission electron microscopy (TEM) image of the nanographite-coated Si specimen at the coating time of 5 min, and it can be found that the coating thicknesses was approximately 40 nm. Due to the fact that the TEM lamellar was prepared at the location near an indentation-induced crack, delamination was observed between the coating and substrate in terms of a bright line. A uniform layer at the top surface of the substrate was also observed, which is a damaged layer caused by a focused ion beam (FIB) milling during making the TEM lamellar. The TEM lamellar of the nanographite-coated Si specimen at the coating time of 15 min was prepared on an original surface. It can be seen from Fig. 2(b) that the coating thickness was approximately 80 nm, and delamination did not occurred. Additionally, the FIB milling-induced uniform damage layer was likewise formed at the top surface of the substrate. For simplicity, the nanographite-coated Si wafers with 5- and 15-min coating times are hereafter referred to as thin-coated and thick-coated specimens, respectively. The detailed parameters of the nanographite coating process are listed in Table 1.

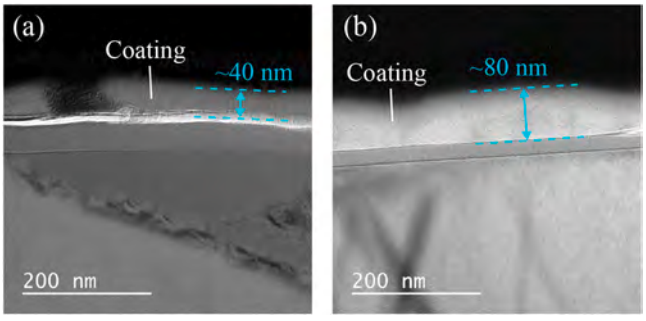

Fig. 2. Cross-sectional TEM images of nanographite-coated Si specimens at the coating time of (a) 5 min, and (b) 15 min.

Table 1
Parameters for the nanographite coating process.

Parameters	Value
Substrate material	Single-crystal silicon (10 × 10 mm)
Thickness	0.525 mm
Surface roughness	< 0.5 nm Sa
Crystal planes	[001]
Silicon source	Silicone rubber (0.5 g)
Carbon source	Benzene 99.9 % (carried by argon 15 SCCM)
Protection gas	Argon 35 SCCM
Temperature	1000 °C
Duration	5, 15 min
Heating rate	10 °C/min

2.2. Design of experiments

Nanoscratching tests were performed on nanographite-coated Si specimens using a nanoindentation-scratching system (Nano Indenter G200, KLA Corporation, USA). During the precision glass molding process, the contact between a glass ball/plate and the nano-graphite-coated Si mold is blunt, and as the mold presses the softened glass, the flow of the softened glass does not cause sharp contact. Therefore, a blunt spherical indenter with the largest tip radius of 10 μm was used for nanoscratching the specimens to better simulate such contact condition. The experiments were performed 10 times at the center of each specimen while a pitch of 40 μm was maintained between each scratch. Two types of nanoscratch tests were conducted. The first method was constant-load nanoscratching. The indenter gradually approached the specimen surface and penetrated it until the normal load reached 10 or 20 mN. Subsequently, the specimen started to move relative to the indenter at a scratching speed of 5 μm/s for a scratching length of 100 μm. During scratching, the normal load was kept constant from the beginning to the end of the scratching. The second method was ramp-load nanoscratching. In this method, the scratching speed and length are the same as that of the first method, but during the movement of the specimen relative to the indenter, the normal load was linearly increased from 0 mN at the beginning to 100 mN at the end of the scratching. All nanoscratching tests were performed under room temperature, as the nanoindentation-scratching system does not have heating functions. The parameters used for the two types of nanoscratching are summarized in Table 2.

The scratched surfaces were observed using field emission scanning electron microscope (FE-SEM, MERLIN Compact, Carl Zeiss AG, Germany). To avoid subtle changes on the surface caused by the electron beam during SEM observation, the acceleration voltage of the electron beam is set to a very low value of 1 kV. Meanwhile, the working distance (WD) is also small at 2.7 mm, and the aperture size is set to 30 μm. The Inlens Duo mode, which activates both secondary electron (SE) and backscattered electron (BSE) detectors, was used to obtain sequential high-resolution topographical and compositional imaging.

Table 2
Parameters for scratching tests under constant load and ramp load.

Parameters	Constant-load scratching	Ramp-load scratching
Specimen	Nanographite-coated Si (5- and 15-min coating time)	
Normal load (P)	10, 20 mN	0–100 mN
Scratching length (L)	100 μm	
Scratching velocity (v)	5 μm/s	
Indenter shape	Spherical indenter (radius of 10 μm)	
Repetition	10 times (pitch of 40 μm)	
Environment	Temperature of 23 °C, and relative humidity of 46 %	

3. Results and discussion

3.1. Grooves under constant loading

Fig. 3(a) and (b) present general views of the grooves scratched on the thin- and thick-coated specimens with a constant load of 10 mN. For both specimens, straight scratched tracks can be observed on the surfaces, which show a bright grey color compared to the pristine coatings that show a dark grey color; none of the scratches produced cracks at the micron scale on the coating surfaces. Typical magnified views of the grooves scratched on the thin and thick coatings, indicated as areas C and D in Fig. 3(a) and (b), respectively, are presented in Fig. 3(c) and (d). A pristine nanographite carbon coating featuring nano-scale island-like domains can be distinctly observed. In the groove scratched on the thin coating, the island-like domains were severely squeezed, resulting in blurry boundaries. In contrast, in the groove scratched on the thick coating, the island-like domains were squeezed and appeared as bright spots, which may have been caused by the indenter rubbing off a small amount of graphite from the coating. The difference in morphology between the two types of grooves resulted in a different color contrast compared to the pristine coating surfaces. Additionally, a few nanoscale cracks can be observed on the coating surface, which propagate along the grain boundaries. Since such nanoscale cracks were also observed in the regions far from the scratched groove, it is considered that these nanoscale cracks are defects on the pristine coating surfaces and were not induced by scratching. This implies that the surface quality of thick coatings is not as good as that of thin coatings, which may result in thick coatings being more susceptible to failure under high-load scratching. Nevertheless, we can still conclude that the grooves on both specimens were formed without generating cracks or significant material removal. In other words, under a constant load of 10 mN, both thin and thick coatings were deformed by burnishing without producing new cracks.

General views of the grooves scratched on the thin- and thick-coated specimens under a constant load of 20 mN are presented in Fig. 4(a) and (b). As shown in Fig. 4(a), the morphologies of the grooves scratched on the thin coating were similar to those of the grooves under a constant load of 10 mN, that is, no cracks occurred on the coating surface. A typical magnified view of a groove on the thin coating, shown in Fig. 4 (c), further confirms that the grooves were produced by burnishing without generating cracks and that a small amount of graphite was rubbed off from the coating, causing the land-like domains to be smudged with bright spots. However, for the grooves scratched on the thick coating, as shown in Fig. 4(b), many cracks were formed in each groove, and the spalling of the coating can also be observed. The shapes of these cracks can be approximately divided into three types, as shown in Fig. 4(d)–(f): forward semi-ring cracks, which open in the same direction as the scratching direction; backward semi-ring cracks, which open in the direction opposite to the scratching direction; and vertical cracks, which propagate perpendicular to the scratching direction. These types of cracks may occur together in one area but are always accompanied by a forward semi-ring crack. The crack patterns were significantly affected by the shape of the indenter [24,25]. For scratching with spherical indenters, the fracture was characterized by the intermittent occurrence of forward semi-ring cracks [26–28]. The formation of such cracks is caused by the Hertzian contact stress under a spherical indenter [29]. When the friction between the indenter and workpiece is low, backward semi-ring cracks may occasionally occur. They are difficult to form at high friction coefficients because under frictionless conditions, the static Hertzian stresses generate annular cracks owing to the tensile stresses at the contact edge of the indenter. With increasing friction, the cracks break open and shift to the trailing side of the contact circle [28]. Since the graphite coatings have proved to be effective solid lubricants [30,31], it is supposed that the graphite coating with a low friction coefficient promotes the formation of backward semi-ring cracks. Vertical cracks formed in response to the tensile stresses generated at the rear of the indenter during sliding, and these

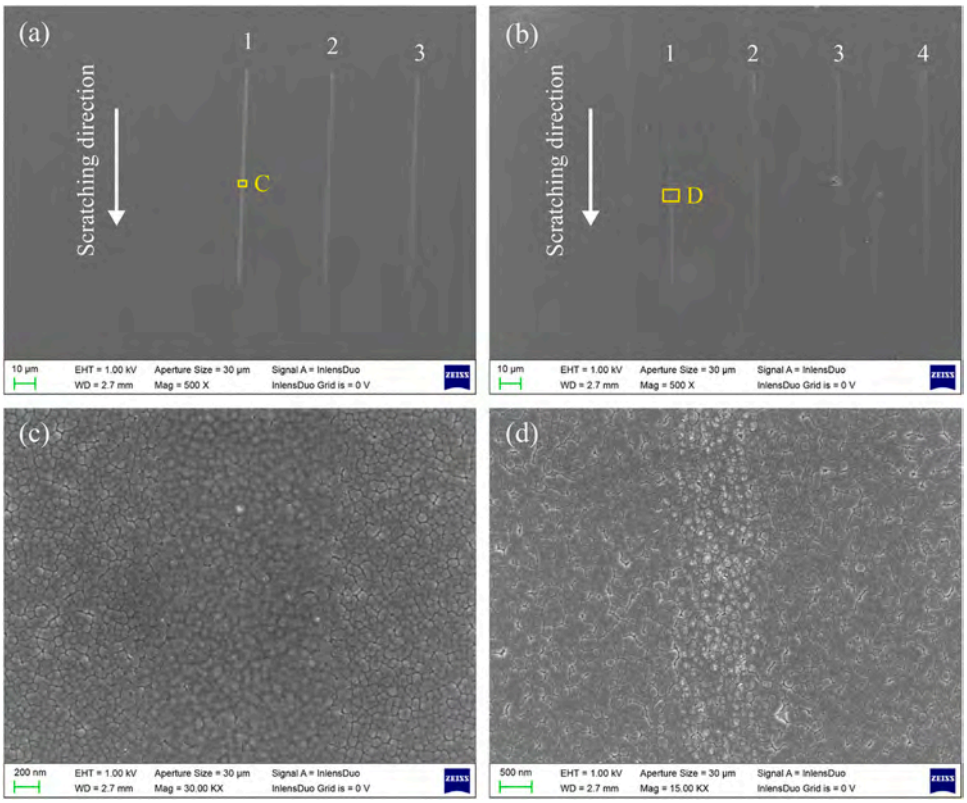

Fig. 3. SEM images of the grooves scratched at the constant load of 10 mN: (a) and (b) are general views of thin-coated and thick-coated specimens; (c) and (d) are magnified views of areas C and D indicated in (a) and (b).

cracks ran perpendicular to the sliding direction with less curvature than the cracks induced by the Hertzian contact stress [32].

Although these cracks may cause spalling of the graphite coating from the Si substrate, no material was removed from the coating to form chips, indicating that the coating was still deformed by burnishing despite the formation of cracks. This is due to the fact that the ratio of scratching depth to the indenter radius is extremely small, while the fracture toughness of the coating is low. Such a phenomenon has also been reported for nanoscratching of other brittle materials with large-radius indenters [33]. The above results show that the critical load for the failure of a thin coating is higher than 20 mN, whereas that for the failure of a thick coating is between 10 mN and 20 mN. In other words, a thinner coating has better resistance to fracture under burnishing conditions.

The penetration depth-scratching distance curves at constant loads are shown in Fig. 5. Five typical curves were plotted for each scratch condition. At a load of 10 mN, the curves of both the thin and thick coatings are extremely smooth, as shown in Fig. 5(a) and (b). This was consistent with the morphologies of the grooves (Fig. 3) where no cracks were generated on the coating surfaces. The penetration depths of the grooves for the thin and thick coatings were approximately 83 nm and 85 nm, respectively, showing good repeatability. The penetration depths for scratching the thin and thick coatings were similar, and the difference was within the margin of error. This indicates that under a small load, the mechanical behaviors of the thin and thick coatings were similar.

The curves of the thin and thick coatings under a load of 20 mN are shown in Fig. 5(c) and (d), respectively. For the thin coating, the curves remained smooth and exhibited good repeatability. The penetration depth was ~115 nm at the beginning of scratching and gradually decreased to ~110 nm at the end, as shown in Fig. 5(c). This may be because some graphite was rubbed off from the coating by the indenter and accumulated in front of the indenter during scratching, which gradually increased the resistance in the direction of the normal load. The groove morphology shown in Fig. 4(c), where the island-like domains are smudged with bright spots of ~1.5 μm in width, supports this argument. In contrast, for the thick coating, all curves started to fluctuate at random positions, as shown in Fig. 5(d). Considering the formation of the cracks observed in Fig. 4(b), it can be inferred that the fluctuations in the curves correspond to the initiation of cracks. Nevertheless, the general penetration depth of the curves was uniform from the beginning to the end of scratching at ~115 nm, indicating that little material accumulated in front of the indenter during scratching. This is also confirmed by Fig. 4(d)–(f), where the island-like domains in the groove are clean. During scratching under the load of 20 mN, cracks formed intermittently on the surface and caused an unstable contact pressure, contributing to a reduction in the amount of material being rubbed off.

Fig. 6(a) shows the atomic force microscopy (AFM) image of the scratched groove on the thin coating at the load of 10 mN. The scratched track is not evident on the 3D topographic map. The cross-sectional profile of the groove along Line A–A′ is shown in Fig. 6(b). It is difficult to distinguish the scratched area from the pristine surface because the cross-sectional profile is generally a flat line with small fluctuations. A similar result was observed for the scratches on the thick coating under the load of 10 mN. This indicates that the load of 10 mN was not sufficiently high to plastically deform the coatings and that the coatings underwent complete elastic recovery after the indenter passed through. When the load was increased to 20 mN, the scratched grooves on the thin coating became evident in the 3D topographic AFM image, as shown in Fig. 7(a1). A groove depth of 4 nm is identified in the cross-sectional profile shown in Fig. 7(a2). In contrast, in the groove on the thick coating under 20 mN, where cracking occurred, the scratch track was not evident, as shown in Fig. 7(b1). The cross-sectional profile along the scratching direction of the groove is plotted in Fig. 7(b2). It can be seen that the warpage of the coating occurred at the head of semi-ring

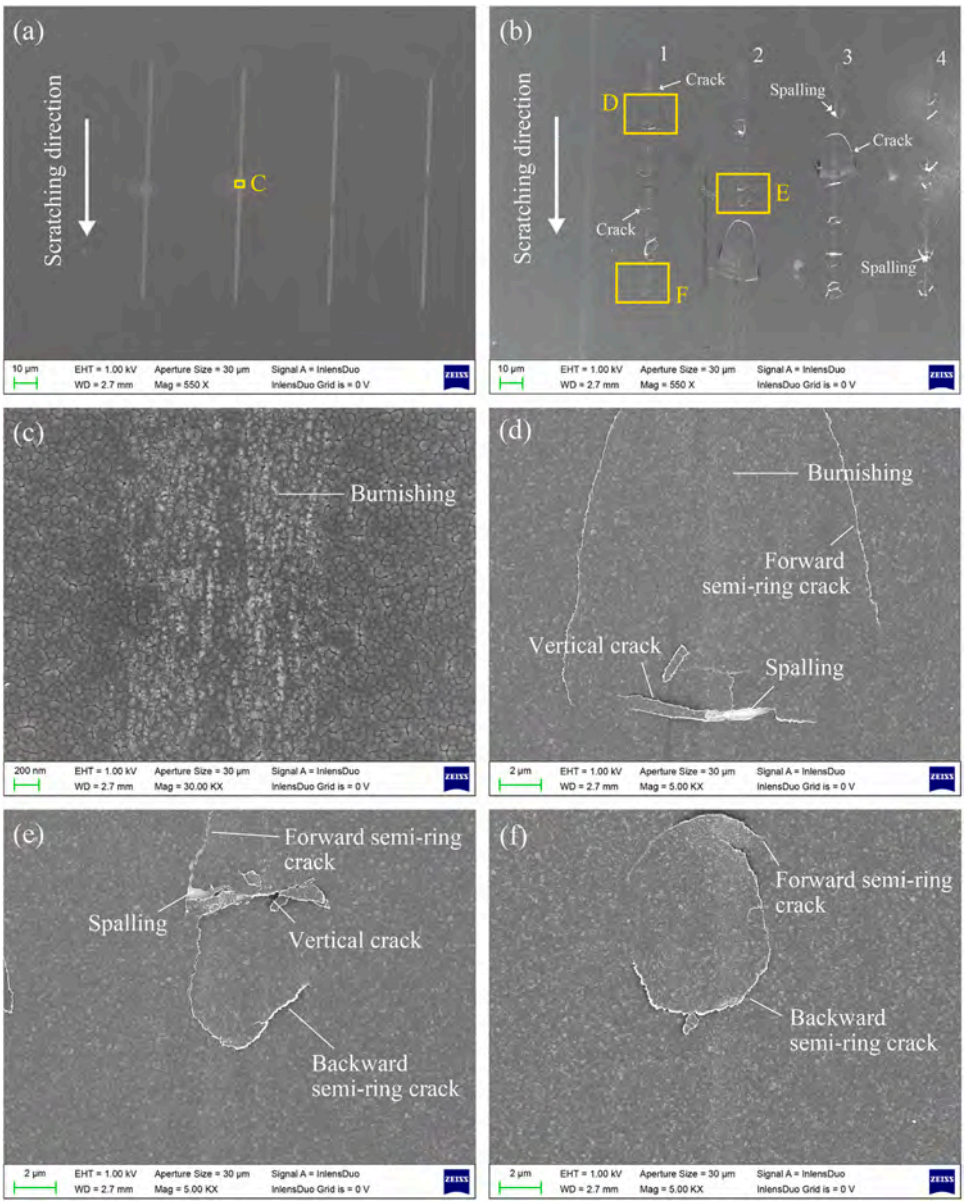

Fig. 4. SEM images of the grooves scratched at the constant load of 20 mN: (a) and (b) are general views of the thin-coated and thick-coated specimens; (c) is a magnified view of Area C indicated in (a); (d)–(f) are magnified views of areas D, E, and F indicated in (b).

cracks, and the height of the area in between the two cracks was slightly higher than the pristine coating surface. This indicates that in the area surrounded by forward and backward semi-ring cracks, the coating lost its adhesion to the specimen.

To analyze the possible phase transformation of the Si substrate after nanoscratching, Raman spectroscopy measurements of the grooves scratched under a constant load of 10 mN on the thin-coated and thick-coated specimens were conducted at the beginning, middle, and end of the grooves where the coating was burnished only. For each specimen, the Raman spectra of each section of the groove were similar; therefore, only one spectrum was plotted for each specimen, as shown in Fig. 8. For both specimens, single-crystal silicon (c-Si) peaks at 520.8 cm^{-1} were clearly observed, indicating that the coating is sufficiently thin to allow the laser to pass through the coating and enter the substrate. No distinct peaks were observed in the Raman shift between 260 cm^{-1} and 521 cm^{-1}, which implies that no phase transformation of Si substrate has occurred after scratching under the load of 10 mN [34,35]. Moreover, the spectra exhibit three obvious peaks, including the D peak at ~1325 cm^{-1}, the G peak at 1597 cm^{-1}, and the broad band at ~2714 cm^{-1}, which indicates the presence of graphite networks with sp^3 and sp^2 carbon bonds [12,36]. The different relative intensities of the 2D peaks were attributed to the different thicknesses of the coatings.

The Raman spectra of the burnished areas of the grooves scratched under 20 mN on the thin- and thick-coated specimens were also characterized, as shown in Figs. 9(a) and 9(b). These spectra show features similar to those obtained in constant-load scratching under 10 mN; however, the relative peak intensities of silicon are slightly greater, which may be attributed to thinner coatings compressed under higher loads. In addition, in the thick-coated specimen the c-Si peak shifted to a higher Raman shift of 522.7 cm^{-1}, indicating higher residual compressive stress in Si substrate [37,38]. Because cracks and spalling occurred in the thick coating, Raman measurements were performed in these areas. In the area of crack formation, the characteristic peaks of Si and nanographite, similar to those shown in Fig. 9(b), were observed, as presented in Fig. 9(c). However, the relative peak intensity of Si decreased slightly. This may be because, after crack formation, the coating lost adhesion to the specimen and then rose slightly, as shown in Fig. 7(b2). Thus, when the laser was focused on the surface of the

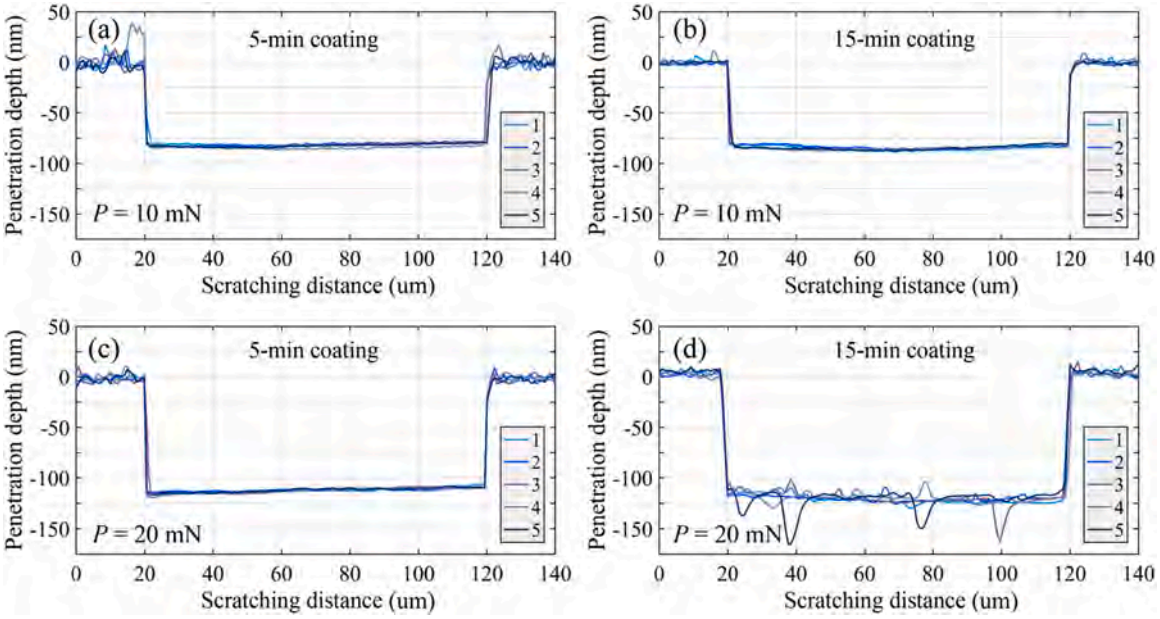

Fig. 5. Curves of penetration depth versus scratching distance: (a) and (b) are the curves under the load of 10 mN on the thin- and thick-coated specimens; (c) and (d) are the curves under the load of 20 mN on the thin- and thick-coated specimens.

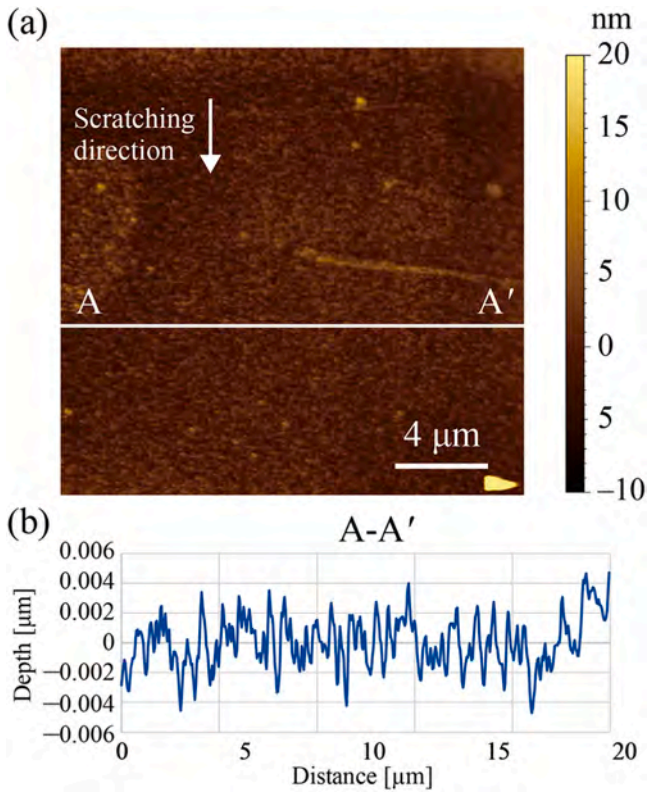

Fig. 6. (a) AFM image of the groove scratched at the constant load of 10 mN on the thin-coated specimen, and (b) cross-sectional profile of the groove along Line A–A′ indicated in (a).

coating, the focal point was farther from the substrate, resulting in a relatively low peak intensity for Si. Moreover, it is found that the Raman shift of the silicon peak returned ~520.8 cm^{-1}, which indicates that less residual compressive stress was induced at the crack area than the burnishing area [37]. This implies that the crack formation consumes a significant amount of energy, resulting in less pressure acting on the substrate. Fig. 9(d) shows the Raman spectrum of the spalling area of the grooves. There are no characteristic peaks of nanographite, and a standard single-crystal silicon spectrum was exhibited; in other words, the main peak of silicon was at ~520.8 cm^{-1}, and no peaks of other phases appeared. This indicated that the microstructure of the Si substrate was barely affected by nanoscratching, even when the normal load was 20 mN.

3.2. *Grooves under ramp loading*

Fig. 10(a) shows a general view of the grooves scratched on the thin-coated specimen under a ramp load with a peak load of 100 mN. Although the scratched track was only marginally visible at the beginning of scratching, it became more apparent and wider as the scratching load increased. None of the scratches produced cracks on the coating surfaces even when the load was increased to 100 mN. Fig. 10(b)–(d) show magnified views of the beginning, middle, and end areas of the scratched groove. At the beginning of the scratching process, the load was low; therefore, fewer materials rubbed off from the coating, resulting in an insignificant scratch track, as shown in Fig. 10(b). As the load increased, the graphite began to rub off the coating, leading to a bright scratch track until the end of the scratching process, as shown in Fig. 10(c) and (d). Crack formation cannot be observed in the high-magnification SEM images.

In contrast, during nanoscratching of the thick-coated specimen at the ramp load with a peak load of 100 mN, the graphite coating was more brittle than the thin-coated specimen. In addition to burnishing, cracks and spalling occurred, as shown in Fig. 11(a). At the beginning of scratching, because the normal load was low, the coating was deformed by burnishing without cracking, similar to the scratching under the constant load of 10 mN. Upon increasing the scratching distance, the load gradually increased and exceeded the critical value of fractures, which was between 10 and 20 mN according to the constant-load scratching tests; consequently, semi-ring cracks began to form in the groove, as shown in Fig. 11(b). As the indenter continued to advance with a further increase in the load, more cracks were generated and intersected with each other, forming a crack network along the edge of the scratch track. These cracks may have been caused by the compressive stress in front of the indenter or the elastic recovery at the rear of the indenter; however, they were all caused by the indenter pressing the

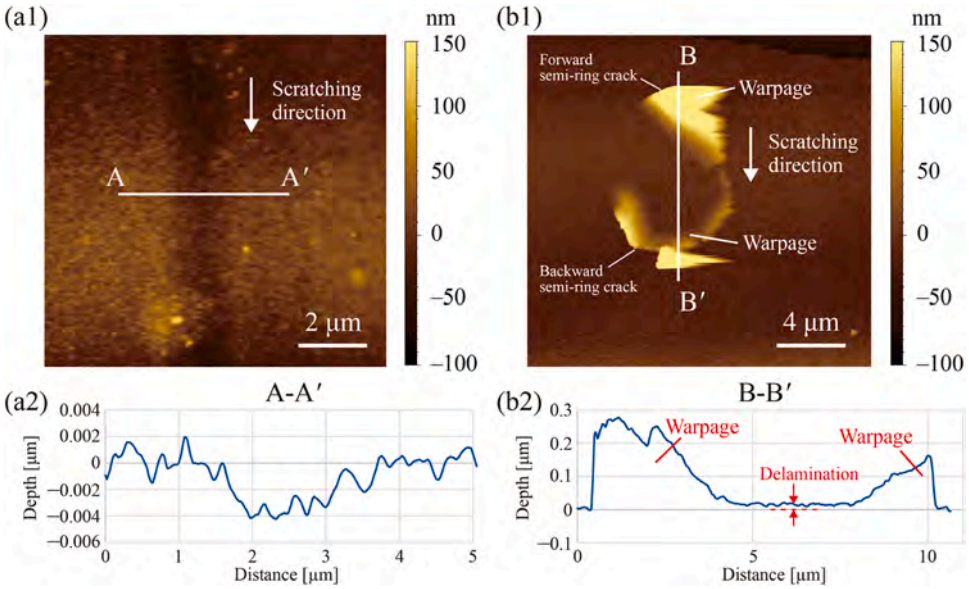

Fig. 7. AFM images of the groove scratched at the constant load of 20 mN on the (a1) thin-coated, and (b1) thick-coated specimens; (a2) and (b2) are the cross-sectional profiles along the lines A–A′ and B–B′ indicated in (a1) and (b1), respectively.

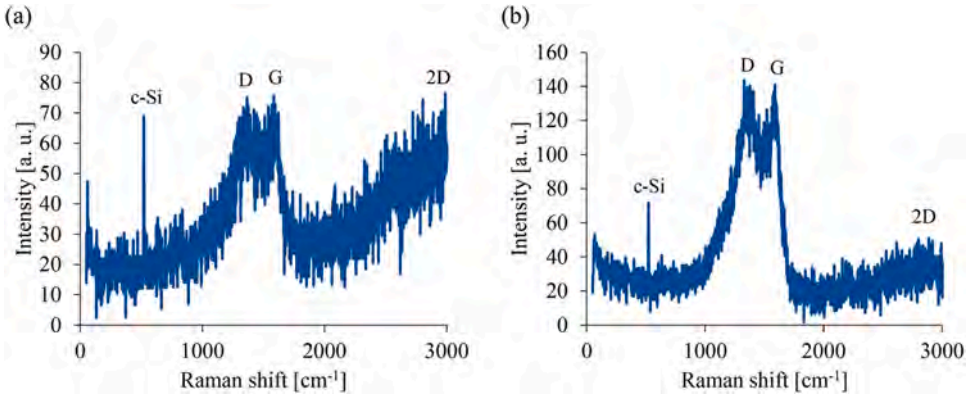

Fig. 8. Raman spectra of the grooves scratched under the constant load of 10 mN on the (a) thin-coated and (b) thick-coated specimens.

surface of the coating. Therefore, when these cracks intersect, significant delamination of small pieces occurs [32]; however, the delaminated coating pieces remain in place, as shown in Fig. 11(c). It is also worth noting from Fig. 11(c) that the scratched track before and after the onset of the press spallation was clearly observed on the Si substrate but disappeared below the delaminated coating piece. This result, on the one hand, confirms that the spalling occurred after the indenter passed over the coating surface, and the coating could protect substrates from severe plastic deformation. On the other hand, it implies that when the load gradually increased to a certain value, the Si substrate below the indenter began to deform and was accompanied by the bending of the coating into the substrate, which led to the delamination and cracks in front of the indenter [39]. Thus, when the indenter continued to move forward, it was in tight contact with the Si substrate once it encountered the spalling caused by the cracks that had formed ahead. Subsequently, large-area spallation was generated because the indenter lifted the coating as it moved forward, as shown in Fig. 11(d). This failure process can be confirmed by the fact that significant burnishing marks were observed on the Si substrate where large-area spallation occurred and that the delaminated coating pieces accumulated at the end of the large-area spallation, as shown in Fig. 11(d). Because the indenter was in direct contact with the substrate when generating lift spallation, scratching was the same as in conventional scratching. In the area of lift spallation, as shown in Fig. 11(e), when the load was increased to ~80 mN, a color change was observed in Si, which was related to the phase transformation. This phase transformation will be addressed later. From the above results, it is known that as the graphite coating thickness increases, failure of the coating becomes more likely.

The penetration depth-scratching distance curves of the thin- and thick-coated specimens at the ramp load are shown in Fig. 12. Five typical curves are plotted for each specimen. For scratching of the thin coating, the curves were extremely smooth with good repeatability, as shown in Fig. 12(a). This was consistent with the morphologies of the grooves (Fig. 10) where no cracks were generated on the coating surfaces. When the thick coating was scratched, the curves started with a stable phase and then began to oscillate as the load increased to approximately 25 mN, as shown in Fig. 12(b). When the load reached 60 mN, the amplitude of the oscillation curve increased. These two changes can be attributed to the fact that cracking and delamination started to occur simultaneously. It is worth noting that when lift spallation occurred in the thick coating, for example, in the second scratch indicated in Fig. 11(a), a sudden increase in the penetration depth was also observed in the corresponding scratch curve, which shifted by ~75 nm in a deeper direction compared to the normal trend of the scratching curve. This height difference is approximately equal to the thickness of the compressed graphite coating. This again indicates that when lift

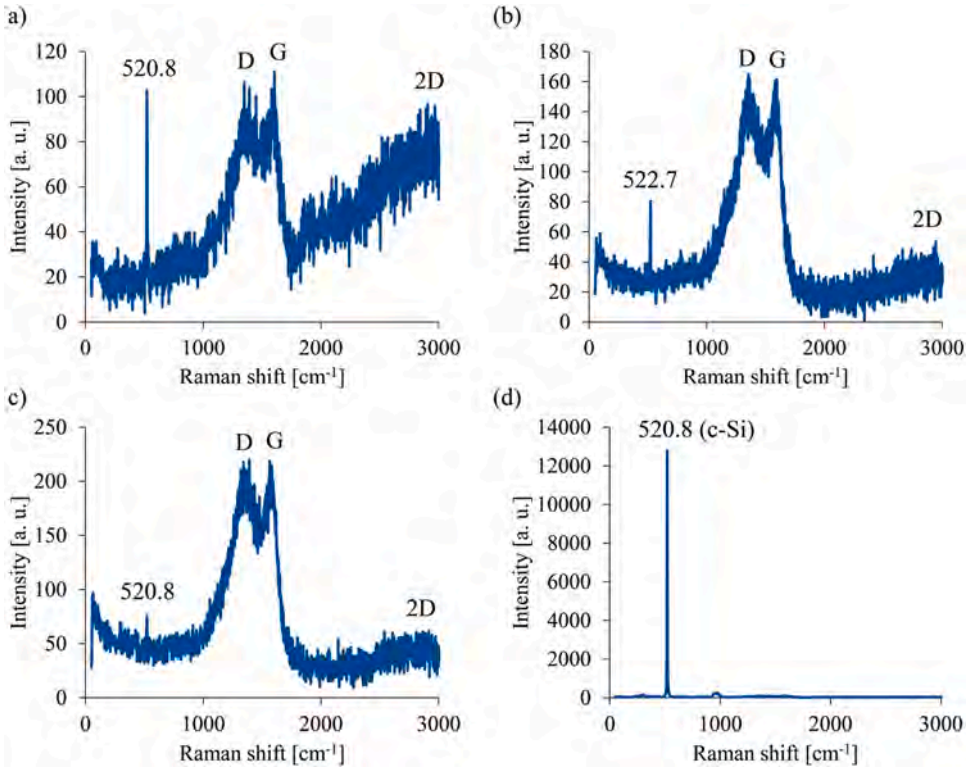

Fig. 9. Raman spectra of the grooves scratched under the constant load of 20 mN measured at (a) burnishing area of the thin-coated specimen; as well as (b) burnishing area, (c) cracking area, and (d) spalling area of the thick-coated specimen.

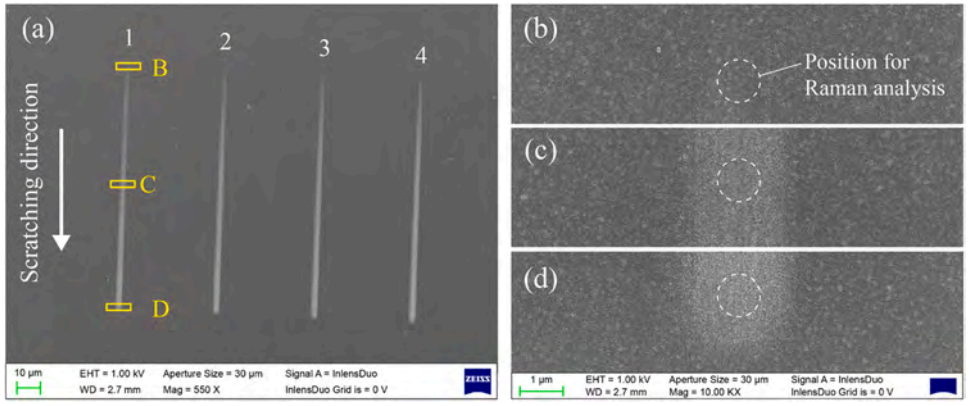

Fig. 10. SEM images of the grooves scratched at the ramp-load with a peak load of 100 mN on the thin-coated specimen: (a) general view of the scratches; (b)–(d) are magnified views of areas B, C, and D indicated in (a).

spallation was generated, the coating was not sandwiched between the indenter and the Si substrate; instead, the indenter was in direct contact with the substrate, and the coating in front of the indenter was lifted as the indenter moved forward.

For the quantitative analysis of the surface topography, sections of the scratched tracks were precisely measured using AFM. For the thin coating, AFM measurements were performed at the beginning and end of the scratch, as shown in Fig. 13(a1) and (b1), respectively. The scratched track was slightly noticeable at the beginning of scratching. The cross-sectional profile shown in Fig. 13(a2) shows that the scratch did not change in the depth direction; however, the scratched areas became relatively flat with a burnishing effect. In contrast, at the end of the scratch, the cross-sectional profile displayed a maximum depth of ~8 nm without distinct pile-ups at the edge of the scratch, as shown in Fig. 13(b2). Considering that the maximum penetration depth during scratching is ~260 nm, as shown in Fig. 12(a), which is much larger than the coating thickness, it can be inferred that the thin graphite coating grown with a 5-min coating time has excellent toughness. Besides, the elastic recovery of the coating was greater than 250 nm, with an elastic recovery rate of approximately 96 %, indicating that the thin coating nearly exhibited elastic behavior even under the burnishing with a load of 100 mN.

For the thick coating, AFM measurements were performed at the first crack area and the lift spallation area in the second scratch (see Fig. 11 (a)). When the load was low, no apparent scratching track was observed in the burnishing area of the thick coating, as shown in Fig. 14(a1). Fig. 14(a2) presents the plots of the cross-sectional profile along Line A–A′, which are difficult to distinguish from the pristine surface, indicating that the thick coating was mainly deformed elastically. The first crack was generated as the load increased. According to the cross-

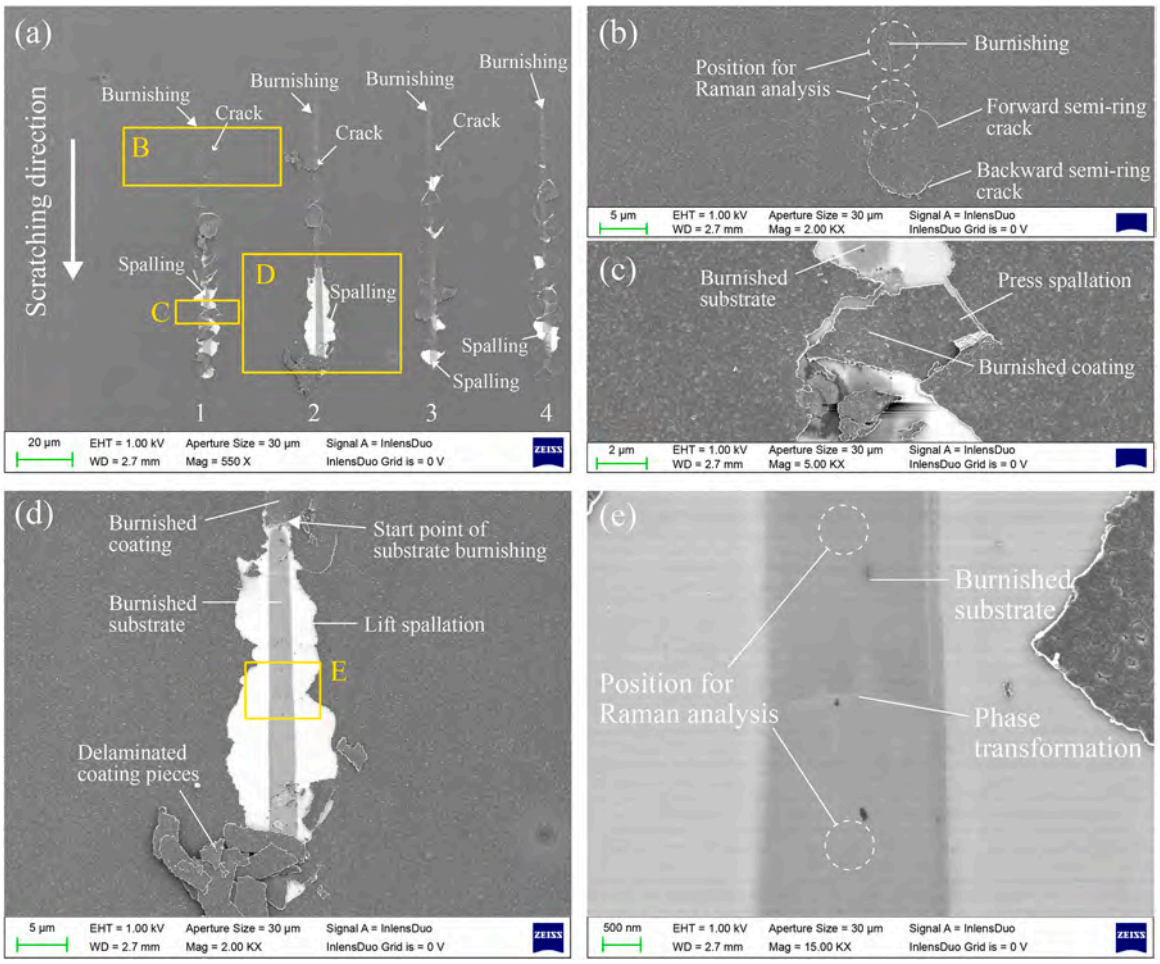

Fig. 11. SEM images of the grooves scratched at the ramp load with a peak load of 100 mN on the thick-coated specimen: (a) general views of the scratches; (b), (c), and (d) are magnified views of areas B, C, and D indicated in (a). (e) is the magnified view of Area E indicated in (d).

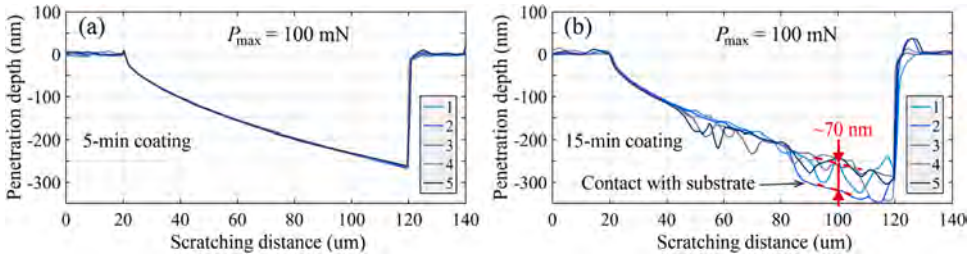

Fig. 12. Curves of penetration depth versus scratching distance at the ramp load with a peak load of 100 mN on the (a) thin-coated and (b) thick-coated specimens.

sectional profile along the scratching direction in the groove, as shown in Fig. 14(a3), the warpage of the coating occurred due to the crack formation and the loss of adhesion of the coating to the substrate. When the load was further increased, lift spallation occurred, as shown in Fig. 14(b1). The cross-sectional profiles located at the initial point of the spallation (Line C–C′) and the spallation area (Line D–D′) are plotted in Fig. 14(b2) and 14(b3). In the C–C′ profile, the height difference between the surface of the coating and the scratched groove was ~90 nm, whereas in D–D′ profile, the height difference decreased to ~80 nm. The decrease of the height difference may be caused by the delaminated coating pieces accumulated in front of the indenter with the scratching, which provided resistance to the load in the normal direction. As a result, the height difference between the groove and substrate surfaces was also not apparent, as shown in Fig. 14(b3). However, owing to lift spallation, the substrate was completely exposed, which enabled the determination of the thickness of the graphite coating grown at the coating time of 15 min. The thickness of the coating was ~80 nm, which was slightly larger than the value determined from the scratching curves in Fig. 12(b). This is because, in Fig. 12(b), the height difference is between the substrate and compressed coating surfaces, which in turn indicates that the coating was plastically deformed by ~10 nm if no failure had occurred.

The Raman spectra of the burnished thin-coated specimen, which were measured at the beginning, middle, and end parts of the scratch presented in Fig. 10 (b)–(d), are depicted in Fig. 15. In general, the spectra of the ramp-load scratches were similar to those of the constant-load scratches on thin coatings, showing distinct peaks of single-crystal silicon and graphite. For the Raman spectra of the beginning and mid areas of the scratch, the Raman shift of c-Si peak was 520.8 cm^{-1}; while for the Raman spectrum of the end area of the scratch, the c-Si peak

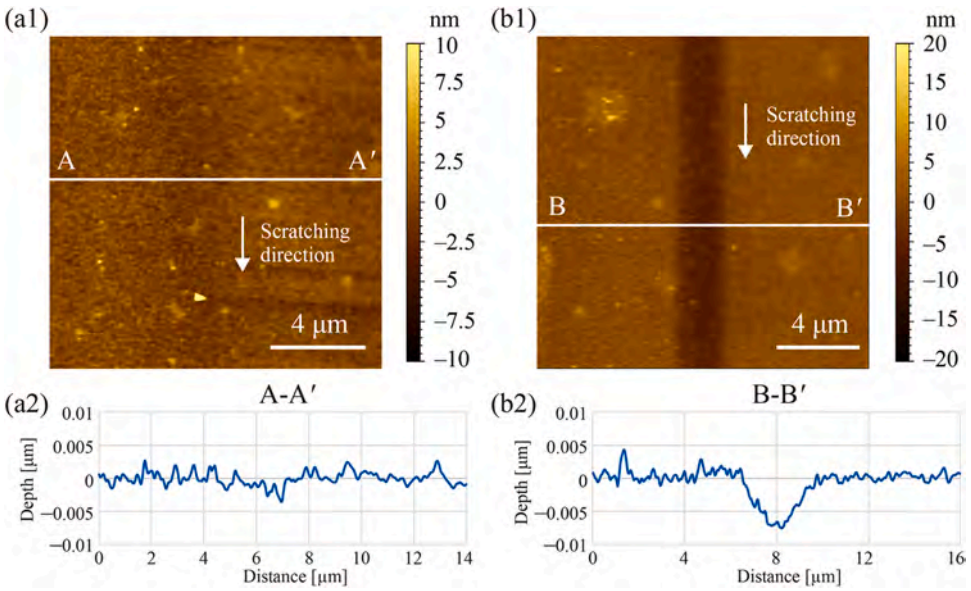

Fig. 13. AFM images of the groove scratched with the ramp load on the thin-coated specimen measured at the (a) beginning and (b) end of the scratch; (a2) and (b2) are the cross-sectional profiles along Line A–A′ and Line B–B′ indicated in (a1) and (b1), respectively.

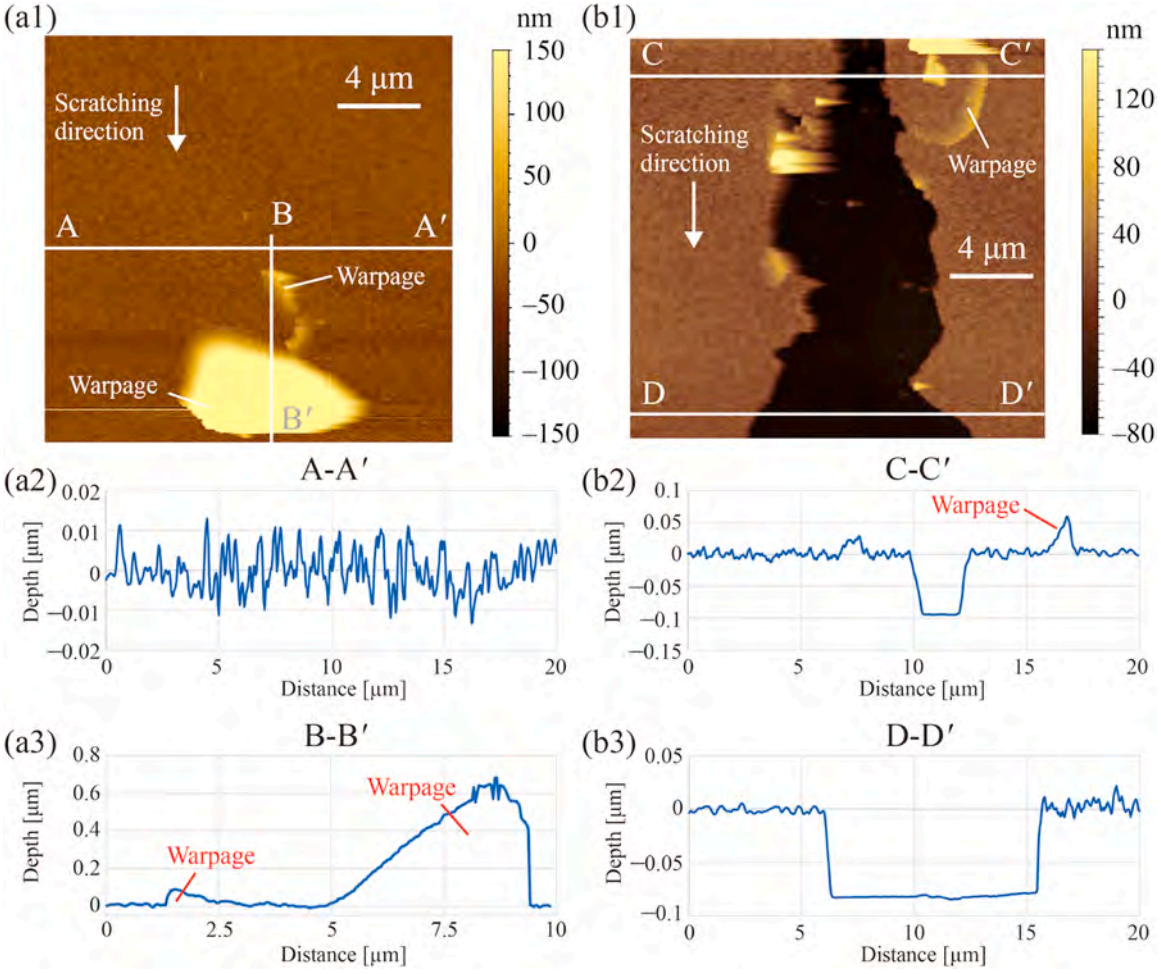

Fig. 14. AFM images of the groove scratched with the ramp load on the thick-coated specimen measured at the area where the (a1) cracks occur, and (b1) lift spallation occurs; (a2, 3) and (b2, 3) are the cross-sectional profiles indicated in (a1) and (b1), respectively.

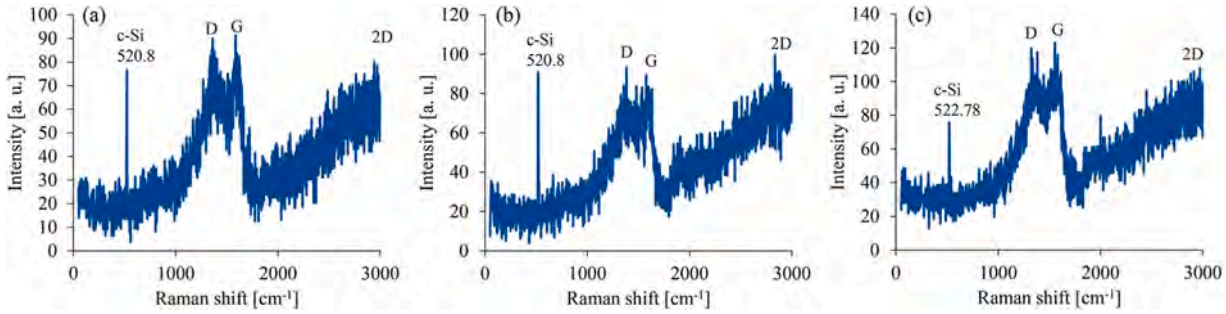

Fig. 15. Raman spectra of the groove scratched at the ramp load on the thin-coated specimen measured at the (a) beginning area, (b) mid area, and (c) end area.

shifted to a higher Raman shift of 522.78 cm^{-1}. These results indicate that a thin graphite coating can protect the substrate from the residual compressive stress when the load does not exceed 50 mN. Moreover, even when a residual compressive stress was generated in the Si substrate under a high load of 100 mN, the Si substrate did not undergo a phase transformation.

The Raman spectra of scratches on the thick-coated specimen were also characterized. The measurement locations included the beginning of the scratch, where the coating was burnished, the area where the first crack occurred, and two spallation areas with different loads, as indicated in Fig. 11(b) and (e). In the burnishing area, peaks for single-crystal silicon (c-Si) and nanographite (D, G, and 2D) were observed, as shown in Fig. 16(a). The intensity of the c-Si was lower than that of the burnished areas of the thin-coated specimen because of the thicker coating covering the substrate. No Si or graphite phase transformations were detected. Fig. 16(b) shows the Raman spectrum of the cracked area, which has features similar to those of the burnished area, except that it exhibits a higher c-Si intensity because the cracks expose the substrate. In the areas of spallation, because the nanographite coating was completely removed from the substrate, the Raman peaks of the nanographite disappeared, as shown in Fig. 16(c) and (d). For the spallation under a load of ~70 mN, a standard single-crystal silicon spectrum with a sharp peak at 520.8 cm^{-1} was observed. The inset shows a peak at around 300 cm^{-1}, which is 2 TA mode of c-Si [40]. In contrast, for the spallation under a load of ~90 mN, the Raman spectrum displays many new peaks. The peak at 470 cm^{-1} indicates the occurrence of amorphous silicon (a-Si)[41]. In addition, the peaks at 166 cm^{-1}, 353 cm^{-1}, and 382 cm^{-1} indicate phase transformations into Si-XII and Si-III phases [35,42]. Because the measurements were performed shortly before and shortly after the color change of the Si described in Fig. 11(e), the color change was believed to be connected with the boundary of the phase transformations, which may be

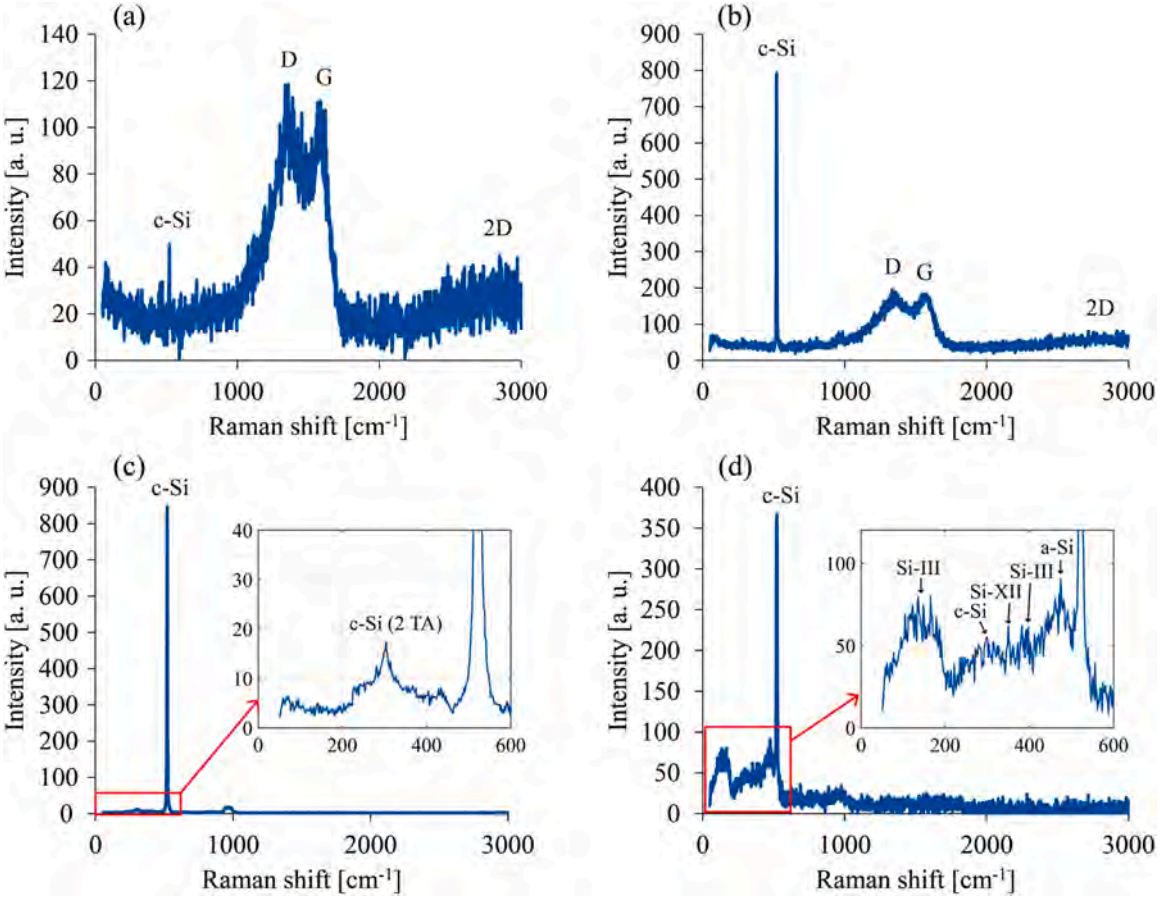

Fig. 16. Raman spectra of the groove scratched at the ramp load on the thick-coated specimen measured at the (a) burnishing area, (b) crack area, (c) spallation area under the load of ~70 mN, and (d) spallation area under the load of ~90 mN.

attributed to the fact that the conductivities of the phase-changed Si and the original single-crystal Si differed [43]. Moreover, the main peak of c-Si shifted to 522.7 cm^{-1}, indicating that compressive residual stress was induced into single-crystal Si [38].

3.3. Phase transformation mechanisms

According to the above results, the critical normal load for the failure of the nanographite coating was significantly determined by the coating thickness. The critical load for crack initiation in the thick coating was lower than that in the thin coating. As shown in Fig. 8, an increase in coating thickness led to a higher intensity ratio of the D peak to the G peak, indicating a reduction in the fraction of sp^3 carbon atoms (diamond structure) and a transition towards sp^2 carbon atoms (graphite structure) in the bonding. This transition resulted in reduced hardness and poor adhesion of the thick coating [44,45]. Consequently, during the scratching of the thin coating, no cracks or other damages occurred. In contrast, in the scratching of the thick coating, as the load increased, cracks gradually initiated and eventually could lead to pressed and lifted spalling, as discussed in Section 3.2. When lift spallation occurred, the indenter established a direct contact with the Si substrate; consequently, phase transformations occurred in the substrate material when the load increased to a certain value. Based on the analysis of the surface morphologies of the scratched surface and the penetration depth-scratching distance curves, a model for the possible phase transformation process was proposed, as illustrated in Fig. 17. As the load gradually increased, the bending of the coating owing to the pressure of the indenter became more severe. Additionally, because of the weaker adhesive strength between the thick coating and the substrate, delamination and consequent cracks occurred in front of the indenter, as shown in Fig. 17(a) [39]. As the indenter continued to move forward, it came into direct contact with the substrate when it moved to the crack location, as supported by the sudden depth change in the scratching curves shown in Fig. 12(b), whereas the coating in front of the indenter was in a state of loss of adhesion to the substrate, as illustrated in Fig. 17(b).

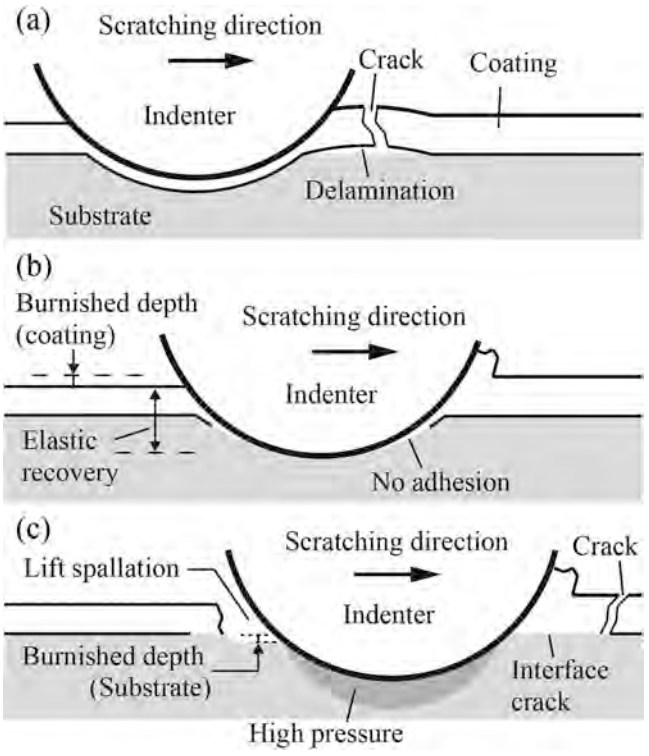

Fig. 17. Schematic model of the substrate phase transformation during lift spallation.

Furthermore, since the indenter was already in direct contact with the substrate, and there was a continuous increase in load, the indenter lifted the coating as it moved forward, causing lift spallation, as shown in Fig. 17(c). In addition, the substrate experienced a higher pressure under the direct indenter-substrate contact than when the coating was sandwiched between the indenter and substrate. When the contact pressure increased with the load to a critical value, a phase transformation of the silicon substrate occurred. However, when a thin coating was scratched, the toughness and elasticity of the coating were high, and the adhesion to the substrate was strong. Thus, the coating tends to recover elastically when subjected to pressure, which counteracts part of the pressure acting on the substrate. Therefore, even if the load acting on the thin coating is greater than that acting on the thick coating, the substrate with the thin coating does not undergo a phase transformation.

4. Conclusion

Constant- and ramp-load nanoscratching tests were performed on nanographite coated single-crystal Si wafers. Two specimens with different coating thicknesses were used: one with a thin coating of ~40 nm (5-min coating time) and the other with a thick coating of ~80 nm (15-min coating time). The deformation and fracture behaviors of the coatings and the phase transformation of the substrate were investigated to understand the failure modes and material responses of the nanographite-on-silicon system. The following can be concluded:

- The critical load for the failure of the coating depends on the coating time and the resulting thickness. The specimen with a thin coating exhibited good toughness and adhesion, whereas that with a thick coating did not. Thus, the critical failure load of the thin coating was significantly greater than that of the thick coating.
- The thin coating was deformed by burnishing without generating cracks on the surface, even when the load was increased to 100 mN. No phase transformations were observed in the Si substrates.
- In the thick coating, the Hertzian contact stress-induced cracks, press spallation, and lift spallation occurred successively with an increasing load. The Hertzian cracks began to appear at loads between 10 and 20 mN. Press and lift spallations formed after the load was increased to 60 mN. The friction coefficient between the indenter and graphite coating was low, causing occasional backward semi-ring cracks.
- Press spallation was generated after the indenter passed over the surface of the coating and was caused by the intersecting cracks. In contrast, lift spallation occurred in front of the indenter as it moved forward owing to the direct contact between the indenter and the Si substrate.
- In the substrate of the specimen with a thick coating, phase transformations into the amorphous, Si-III and Si-XII phases were identified in the area of lift spallation when the load was increased to 80 mN.

These findings indicate that thin coatings have better mechanical resistance under blunt contact, which protects the substrate from phase transformations. This study provides guidance for the preparation of coated molds in the glass molding industry and for other applications using coating protection. As the microstructural changes in the coatings are also important for applications, efforts on detailed characterizations of the nanographite coating will be made in the future to understand the nanoscale and even atomic scale microstructure evolution under mechanical loads. In addition, some applications of the nanographite coating, such as glass molding, are conducted at high-temperature environments. These harsh conditions can potentially result in premature failure for both thick and thin coatings, with a particular susceptibility in the thick coating due to its inherently weak adhesion. Therefore, as part of future work, it is essential to determine the thresholds of the

nanographite coating failures and understand the coating's deformation behavior when subjected to mechanical loads at elevated temperatures.

CRediT authorship contribution statement

Fabian Brüssel: Data curation, Formal analysis, Investigation, Methodology, Writing – original draft. **Weihai Huang:** Data curation, Formal analysis, Investigation, Methodology, Validation, Visualization, Writing – original draft. **Jiwang Yan:** Conceptualization, Methodology, Funding acquisition, Project Management, Resources, Supervision, Writing – review & editing.

Declaration of Competing Interest

The authors declare that they have no known competing financial interests or personal relationships that could have appeared to influence the work reported in this paper.

Data availability

Data will be made available on request.

References

[1] Liu Q, He Y, Yan J, Chen Z, Zhao C, Zhou H. Large-area vapor-deposited Cs3Cu2I5 perovskite thin films for highly effective third-order nonlinear optics. J Alloy Compd 2023;vol. 933:167606. https://doi.org/10.1016/j.jallcom.2022.167606.

[2] Mishra J, et al. Mid-infrared nonlinear optics in thin-film lithium niobate on sapphire. Optica 2021;vol. 8(6):921–4. https://doi.org/10.1364/OPTICA.427428.

[3] Bobzin K, Kalscheuer C, Möbius MP, Rank M, Oehler M, Koch O. Triboactive coatings for wear and friction reduction in chain drives. Tribology Int 2023;vol. 185:108562. https://doi.org/10.1016/j.triboint.2023.108562.

[4] Fang W, Chen J, Cai F, Zhou Q, Li M, Zhang S. Reduced crater wear and improved high-speed dry cutting performance of B-containing AlTiBN coatings against Ti-6Al-4 V alloy. Tribology Int 2023;vol. 187:108730. https://doi.org/10.1016/j.triboint.2023.108730.

[5] Frutos E, Richhariya V, Silva FS, Trindade B. Manufacture and mechanical-tribological assessment of diamond-reinforced Cu-based coatings for cutting/grinding tools. Tribology Int 2023;vol. 177:107947. https://doi.org/10.1016/j.triboint.2022.107947.

[6] Liang H, Shi B, Fairchild A, Cale T. Applications of plasma coatings in artificial joints: an overview. Vacuum 2004;vol. 73(3):317–26. https://doi.org/10.1016/j.vacuum.2003.12.160.

[7] Akhtar A, Ruan H. Review on thin film coatings for precision glass molding. Surf Interfaces 2022;vol. 30:101903. https://doi.org/10.1016/j.surfin.2022.101903.

[8] Han JH, et al. Chemical Vapor Deposition of Ru Thin Films with an Enhanced Morphology, Thermal Stability, and Electrical Properties Using a RuO4 Precursor. Chem Mater 2009;vol. 21(2):207–9. https://doi.org/10.1021/cm802485r.

[9] Liu S-C, et al. The chemical inertness of Ir–Re and Ta–Ru coatings in molding B2O3–ZnO–La2O3-based glass. Surf Coat Technol 2014;vol. 259:352–7. https://doi.org/10.1016/j.surfcoat.2014.01.061.

[10] Zhang L, Yi AY. Investigation of mid-infrared rapid heating of a carbide-bonded graphene coating and its applications in precision optical molding. Opt Express 2021;vol. 29(19):30761–71. https://doi.org/10.1364/OE.405603.

[11] He Peng, et al. Graphene-coated Si mold for precision glass optics molding. Opt Lett 2013;vol. 38(14):2625–8. https://doi.org/10.1364/OL.38.002625.

[12] Zhang L, Yan J. Study on nano-graphitic carbon coating on Si mold insert for precision glass molding. Surf Coat Technol 2022;vol. 448:128893. https://doi.org/10.1016/j.surfcoat.2022.128893.

[13] Yan J, Zhou T, Masuda J, Kuriyagawa T. Modeling high-temperature glass molding process by coupling heat transfer and viscous deformation analysis. Precis Eng 2009;vol. 33(2):150–9. https://doi.org/10.1016/j.precisioneng.2008.05.005.

[14] Zhang L, Yan J. Amorphous carbon coated silicon wafer as mold insert for precision glass molding. Procedia CIRP 2022;vol. 108:525–30. https://doi.org/10.1016/j.procir.2022.03.082.

[15] Beake BD, Vishnyakov VM, Harris AJ. Relationship between mechanical properties of thin nitride-based films and their behaviour in nano-scratch tests. Tribology Int 2011;vol. 44(4):468–75. https://doi.org/10.1016/j.triboint.2010.12.002.

[16] Bull SJ, Berasetegui EG. An overview of the potential of quantitative coating adhesion measurement by scratch testing. Tribology Int 2006;vol. 39(2):99–114. https://doi.org/10.1016/j.triboint.2005.04.013.

[17] Beake BD, Vishnyakov VM, Valizadeh R, Colligon JS. Influence of mechanical properties on the nanoscratch behaviour of hard nanocomposite TiN/Si3N4 coatings on Si. J Phys D: Appl Phys 2006;vol. 39(7):1392. https://doi.org/10.1088/0022-3727/39/7/009.

[18] Beake BD, Vishnyakov VM, Harris AJ. Nano-scratch testing of (Ti,Fe)Nx thin films on silicon. Surf Coat Technol 2017;vol. 309:671–9. https://doi.org/10.1016/j.surfcoat.2016.11.024.

[19] Lee J-E, Kim H-J, Kim D-E. Assessment of adhesion between thin film and silicon based on a scratch test. J Mech Sci Technol 2010;vol. 24(1):97–101. https://doi.org/10.1007/s12206-009-1124-7.

[20] Li X, Bhushan B. Micro/nanomechanical and tribological characterization of ultrathin amorphous carbon coatings. J Mater Res 1999;vol. 14(6):2328–37. https://doi.org/10.1557/JMR.1999.0309.

[21] Wu YQ, Huang H, Zou J, Zhang LC, Dell JM. Nanoscratch-induced phase transformation of monocrystalline Si. Scr Mater 2010;vol. 63(8):847–50. https://doi.org/10.1016/j.scriptamat.2010.06.034.

[22] Gogotsi Yury, Zhou Guohui, Ku Sang-Song, Cetinkunt Sabri. Raman microspectroscopy analysis of pressure-induced metallization in scratching of silicon. Semicond Sci Technol 2001;vol. 16(5):345. https://doi.org/10.1088/0268-1242/16/5/311.

[23] Tao H, Zeng Q, Liu Y, Zhao D, Lu X. Influence of anisotropy on material removal and deformation mechanism based on nanoscratch tests of monocrystal silicon. Tribology Int 2023;vol. 187:108736. https://doi.org/10.1016/j.triboint.2023.108736.

[24] Lawn BR, Borrero-Lopez O, Huang H, Zhang Y. Micromechanics of machining and wear in hard and brittle materials. J Am Ceram Soc 2021;vol. 104(1):5–22. https://doi.org/10.1111/jace.17502.

[25] Huang W, Yan J. Effect of tool geometry on ultraprecision machining of soft-brittle materials: a comprehensive review. Int J Extrem Manuf 2023;vol. 5(1):12003. https://doi.org/10.1088/2631-7990/acab3f.

[26] Geng X, Zhang Z, Barthel E, Dalmas D. Mechanical behavior of stiff coating on glass under sliding contact. Wear 2010;vol. 269(5):351–61. https://doi.org/10.1016/j.wear.2010.04.016.

[27] Lee K, Marimuthu KP, Kim C-L, Lee H. Scratch-tip-size effect and change of friction coefficient in nano / micro scratch tests using XFEM. Tribology Int 2018;vol. 120:398–410. https://doi.org/10.1016/j.triboint.2018.01.003.

[28] Leu HJ, Scattergood RO. Sliding contact fracture on glass and silicon. J Mater Sci 1988;vol. 23(8):3006–14. https://doi.org/10.1007/BF00547483.

[29] Lawn BR. Indentation of ceramics with spheres: a century after hertz. J Am Ceram Soc 1998;vol. 81(8):1977–94. https://doi.org/10.1111/j.1151-2916.1998.tb02580.x.

[30] Qi J, Liu H, Luo Y, Zhang D, Wang Y. Influences of added sand-dust particles on the tribological performance of graphite-like coating under solid–liquid lubrication. Tribology Int 2014;vol. 71:69–81. https://doi.org/10.1016/j.triboint.2013.11.003.

[31] Mandal P, Ehiasarian AP, Hovsepian PE. Lubricated sliding wear mechanism of chromium-doped graphite-like carbon coating. Tribology Int 2014;vol. 77:186–95. https://doi.org/10.1016/j.triboint.2014.04.007.

[32] Bull SJ. Failure modes in scratch adhesion testing. Surf Coat Technol 1991;vol. 50(1):25–32. https://doi.org/10.1016/0257-8972(91)90188-3.

[33] Huang W, Yan J. Chip-free surface patterning of toxic brittle polycrystalline materials through micro/nanoscale burnishing. Int J Mach Tools Manuf 2021;vol. 162:103688. https://doi.org/10.1016/j.ijmachtools.2020.103688.

[34] Huang W, Yan J. Towards understanding the mechanism of vibration-assisted cutting of monocrystalline silicon by cyclic nanoindentation. J Mater Process Technol 2023;vol. 311:117797. https://doi.org/10.1016/j.jmatprotec.2022.117797.

[35] Gogotsi Y, Baek C, Kirscht F. Raman microspectroscopy study of processing-induced phase transformations and residual stress in silicon. Semicond Sci Technol 1999;vol. 14(10):936. https://doi.org/10.1088/0268-1242/14/10/310.

[36] Alhwaige AA, Alhassan SM, Katsiotis MS, Ishida H, Qutubuddin S. Interactions, morphology and thermal stability of graphene-oxide reinforced polymer aerogels derived from star-like telechelic aldehyde-terminal benzoxazine resin. RSC Adv 2015;vol. 5(112):92719–31. https://doi.org/10.1039/C5RA16188F.

[37] Parker JH, Feldman DW, Ashkin M. Raman scattering by silicon and germanium. Phys Rev 1967;vol. 155(3):712–4. https://doi.org/10.1103/PhysRev.155.712.

[38] Weinstein BA, Piermarini GJ. Raman scattering and phonon dispersion in Si and GaP at very high pressure. Phys Rev B 1975;vol. 12(4):1172–86. https://doi.org/10.1103/PhysRevB.12.1172.

[39] Holmberg K, Laukkanen A, Ronkainen H, Wallin K, Varjus S, Koskinen J. Tribological contact analysis of a rigid ball sliding on a hard coated surface: Part I: modelling stresses and strains. Surf Coat Technol 2006;vol. 200(12):3793–809. https://doi.org/10.1016/j.surfcoat.2005.03.040.

[40] Igor Iatsunskyi, Stefan Jurga, Valentyn Smyntyna, Mykolai Pavlenko, Valeriy Myndrul, and Anastasia Zaleska, "Raman spectroscopy of nanostructured silicon fabricated by metal-assisted chemical etching," in 2014, p. 913217.

[41] Domnich V, Gogotsi Y. Phase transformations in silicon under contact loading. Rev Adv Mater Sci 2002;(3).

[42] Pizani PS, Jasinevicius RG, Zanatta AR. Effect of the initial structure of silicon surface on the generation of multiple structural phases by cyclic microindentation. Appl Phys Lett 2006;vol. 89(3):31917. https://doi.org/10.1063/1.2227644.

[43] Ruffell S, Bradby JE, Williams JS, Warren OL. An in situ electrical measurement technique via a conducting diamond tip for nanoindentation in silicon. J Mater Res 2007;vol. 22(3):578–86. https://doi.org/10.1557/jmr.2007.0100.

[44] Shi X, Liskiewicz TW, Beake BD, Chen J, Wang C. Tribological performance of graphite-like carbon films with varied thickness. Tribology Int 2020;vol. 149:105586. https://doi.org/10.1016/j.triboint.2019.01.045.

[45] Wei C, Yen J-Y. Effect of film thickness and interlayer on the adhesion strength of diamond like carbon films on different substrates. Diam Relat Mater 2007;vol. 16(4):1325–30. https://doi.org/10.1016/j.diamond.2007.02.003.